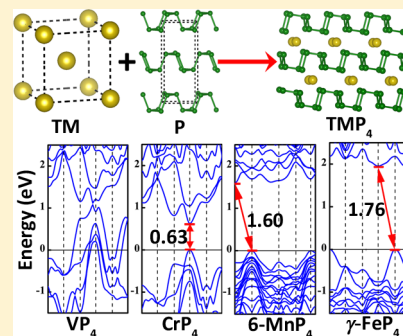


Structural Diversity and Electronic Properties of 3d Transition Metal Tetraphosphides, TMP_4 (TM = V, Cr, Mn, and Fe)Ning Gong,[†] Chunxing Deng,[†] Lailei Wu,^{*,†,§} Biao Wan,^{†,‡} Zhibin Wang,[§] Zhiping Li,[§] Huiyang Gou,^{*,‡,§} and Faming Gao[§]HPSTAR
674-2018[†]State Key Laboratory of Metastable Materials Science and Technology, College of Material Science and Engineering, Yanshan University, Qinhuangdao 066004, China[‡]Center for High Pressure Science and Technology Advanced Research, Beijing 100094, China[§]Key Laboratory of Applied Chemistry, College of Environmental and Chemical Engineering, Yanshan University, Qinhuangdao 066004, China

Supporting Information

ABSTRACT: Transition-metal (TM) phosphides attract increasing attention with applications for energy conversion and storage, due to their outstanding physical, chemical, and electronic properties. The 3d transition metal tetraphosphides (TMP_4 , TM = V, Cr, Mn, and Fe) possess multiple allotropies and rich electronic properties. Here, we perform the investigations of the structural, electronic, and elastic properties for 3d- TMP_4 (TM = V, Cr, Mn, and Fe) using density functional theory (DFT) calculations. These compounds are featured with alternating buckled phosphorus sheets with ten-numbered phosphorus rings and varied transition-metal layers. Hybrid DFT calculations reveal that TMP_4 compounds exhibit a wide range of electrical properties, ranging from metallic behavior for VP_4 to semiconducting behavior for CrP_4 with the narrow direct band gap of 0.63 eV to enlarged semiconducting MnP_4 and FeP_4 with band gap of 1.6–2.1 eV. The bonding analysis indicates that P–P and TM–P covalent interactions dominate in the phosphorus sheets and TMP_6 octahedrons, which are responsible for the structural and electronic diversity.



INTRODUCTION

Transition-metal phosphides (TMPs), in particular, phosphorus-rich phases, have attracted considerable interest due to the earth-abundance and outstanding properties, such as high activity, good electrical conductivity, and high lithium capacity.^{1–4} For instance, FeP and FeP_2 nanowires (NWs) exhibit excellent performance for hydrogen evolution reduction (HER) in both strong acidic and basic aqueous solutions.⁵ Moreover, improved electrocatalytic efficiency and better durability were achieved for FeP_2 NWs in comparison with the FeP NWs because of the more negatively charged P anions for active proton-acceptor sites and the high efficiency of the richer P composition protecting metal ions against oxidation. High efficiency for HER or oxygen evolution reaction (OER) or both was also reported for CoP ,⁶ MoP_2 ,⁷ and CoP_3 ⁸ because of the good stability of TMPs in acidic and basic media superior to their pure metal counterparts. The charge transfer between the TM and P atoms is critical for the electrocatalysis process, which promotes the adsorption and desorption of reactant and product molecules. For HER, the positively charged TM centers and the negatively charged basic P centers could act as the hydride acceptor and proton acceptor centers, respectively, and P centers can promote the formation of TM-hydride, facilitating the following hydrogen evolution by electrochemical desorption. While for OER, the same principle

may be adopted that the metal sites in TMPs act as hydroxyl acceptor and the phosphorus sites promote the adsorption of hydroxyl on TM centers then in favor of oxygen evolution through discharging and desorption.

CrP_4 was first synthesized by reaction of the constituent elements at pressure of 1.5–6.5 GPa about half century ago.⁹ Later on, 3d transition-metal tetraphosphides (TMP_4) of VP_4 ,¹⁰ MnP_4 ,^{11–14} and FeP_4 ^{15–17} were prepared by high pressure or chemical transport with iodine or bromine at high temperature. The 3d TMP_4 compounds crystallize in different crystal symmetry with covalent phosphorus networks, where the cavities or channels may facilitate the migration of lithium ion. The low-potential intercalation of lithium into MnP_4 was first reported by Souza et al. in 2002,¹⁸ followed by the report on topotactic intercalation of Li_xVP_4 compounds by Doublet et al.¹⁹ Since then, numerous investigations have been performed on the insertion/extraction of lithium into 3d transition-metal phosphides, such as VP_4 ,²⁰ NiP_2 ,^{21,22} FeP_2 ,^{23,24} CoP_3 ,^{25,26} and TiP_2 .²⁷ The high gravimetric and volumetric capacities (500–1800 mAh g^{-1}) make them able to be alternative anode materials for lithium ion battery (LIB).²⁸ So far, however, most studies were focused on the physical and chemical properties

Received: May 20, 2018

Published: July 19, 2018

Table 1. Lattice Parameters of TMP_4 in Comparison with Experimental Results, Relative Formation Enthalpy, ΔE_f , and Calculated Band Gap, E_g^a

phase	SG	<i>a</i>	<i>b</i>	<i>c</i>	α	β	γ	ΔE_f	PBE- E_g	HSE- E_g	ref
VP ₄	C2/c	5.216	11.007	5.802		110.3					
		5.259	10.997	5.879		110.87					exptl ¹⁰
CrP ₄	C2/c	5.170	10.684	5.692		110.3				0.63	
		5.191	10.760	5.771		110.648					exptl ⁹
6-MnP ₄	$\bar{P}1$	16.288	5.831	5.082	115.5	95.3	89.2	0	0.47	1.60	
		16.347	5.847	5.108	115.66	95.15	89.21				exptl ¹²
8-MnP ₄	C2/c	10.485	5.069	21.693		94.6		0.003	0.53	1.76	
		10.513	5.094	21.804		94.71					exptl ¹³
2-MnP ₄	$\bar{P}1$	5.847	5.080	5.814	93.6	107.4	115.8	0.009	0.40	1.62	
		5.847	5.080	5.814	93.61	107.37	115.78				exptl ¹¹
γ -MnP ₄	Cc	5.084	10.503	10.855		93.6		0.036	0.51	1.83	
		5.105	10.540	10.875		93.80					exptl ¹⁴
γ -FeP ₄	C2/c	4.993	10.311	11.027		90.8		0	0.77	1.76	
		5.054	10.407	11.069		91.14					exptl ¹⁷
α -FeP ₄	P2 ₁ /c	4.577	13.543	6.947		101.4		0.011	0.87	2.13	
		4.619	13.67	7.002		101.48					exptl ¹⁵
β -FeP ₄	C222 ₁	4.949	10.145	5.486				0.064	0.88	1.83	
		5.005	10.213	5.30							exptl ¹⁶

^a*a*, *b*, and *c* in Å; α , β , and γ in deg. TM = V, Cr, Mn, and Fe. ΔE_f in eV/fu. E_g in eV.

of TMPs for their practical applications. Theoretical investigations on the crystal structures and chemical bonding of TMPs, especially for TMP_4 are scarce.²⁹ Theoretical calculations can provide useful information for the understanding of phase stability and elastic and electronic properties of the phosphides. For example, CoP and IrP were calculated via first-principles calculations,^{30–32} and the optoelectronic properties were revealed for IrP. Elastic, magnetic, and electronic properties of Ir₂P were also calculated.³³ In addition, TaP was studied theoretically to understand the Weyl semimetal feature by Xu et al.³⁴ In this work, the systematic investigations on the structure, chemical bonding, and elastic properties of 3d TMP_4 (TM = V, Cr, Mn, and Fe) were performed using first-principles calculations. Our findings may inspire further explorations of TMP_4 applications.

COMPUTATIONAL METHODS

Our geometry optimizations were performed within the Cambridge Serial Total Energy Package (CASTEP) code,³⁵ based on density functional theory (DFT). For the exchange-correlation functional, we employed the generalized gradient approximation functional developed by Perdew, Burke, and Ernzerhof (GGA-PBE).³⁶ A plane-wave basis set cutoff energy of 500 eV was chosen and a dense Monkhorst–Pack *k*-point grid of spacing $2\pi \times 0.03 \text{ \AA}^{-1}$ was used for the Brillouin zone to ensure the convergence of total energy less than 1 meV per atom. All the compounds were fully relaxed until the differences of the total energy were less than 1.0×10^{-5} eV, and atomic forces were within 1×10^{-3} eV/Å. The band structures and density of states (DOS) calculations were performed with the Vienna Ab initio Simulation Package (VASP),³⁷ based on DFT with Heyd–Scuseria–Ernzerhof (HSE06) hybrid functional. Crystal orbital Hamilton population (COHP)³⁸ was calculated for bonding features, and the electron transfer via the Bader charge scheme³⁹ was also calculated. Mulliken overlap populations (MOP) were calculated using CASTEP code. The elastic constants (C_{ij}) were determined by calculating the stress tensor driven by strain changes. The bulk modulus (*B*), shear modulus (*G*) and Young's modulus (*E*) were evaluated by the method of Voigt–Reuss–Hill (VRH)⁴⁰ approximation. Crystal structure figures were plotted using VESTA package.⁴¹

RESULTS AND DISCUSSION

Structure and Stability. The calculated lattice parameters and relative formation enthalpy (ΔE_f) of 3d TMP_4 are presented in Table 1 in comparison with available experimental results. The relative formation enthalpies for MnP_4 and FeP_4 modifications are defined as $\Delta E_f^{\text{MnP}_4} = E_f(\text{MnP}_4) - E_f(6\text{-MnP}_4)$, and $\Delta E_f^{\text{FeP}_4} = E_f(\text{FeP}_4) - E_f(\gamma\text{-FeP}_4)$. The deviations between the experimental and calculated values are within the typical DFT errors ($\sim 2\%$). As listed in Table 1, 6-MnP₄ and γ -FeP₄ show the lowest formation enthalpy ($\Delta E_f = 0$) among different configurations of MnP_4 and FeP_4 , respectively. Moreover, the phase formation of 6-MnP₄, 8-MnP₄, and 2-MnP₄ is very competitive during synthesis due to small energy difference within 10 meV/fu, in good agreement with previous experiment observations.^{11–13} For γ -MnP₄, the metastable nature is revealed by its formation enthalpy, higher than that of 6-MnP₄ by 36 meV/fu; this agrees well with the high annealing temperature (923–1073 K) during synthesis, and it is difficult to separate from the mixture of manganese tetraphosphides.¹⁴ For iron tetraphosphide (FeP_4), the formation enthalpy of α -FeP₄ is close to that of γ -FeP₄ (higher by about 11 meV/fu), whereas β -FeP₄ is higher than γ -FeP₄ by about 64 meV/fu, agreeing with the synthesis at high temperature and high pressure conditions (1373 K and 6 GPa) for β -FeP₄.¹⁶ Additionally, the calculated phase transition can be found for FeP_4 in Figure 1, γ -FeP₄ transforms into α -phase at 2.8 GPa then to β -phase at 4.9 GPa. The transition pressure can be easily reached by the current capability of high-pressure techniques; further verification is expected.

The crystal structures of 3d TMP_4 (TM = V, Cr, Mn, and Fe) are shown in Figures 2 and 3. All the phases could be seen as the black phosphorus⁴² layered structure (Figure 2i) intercalated by the TM atoms, accompanied by reordering of atomic stacks from AB to AC, similar to that of Na intercalating into black phosphorus.⁴³ Besides, due to the intercalation of TM atoms, the sharing edge of the two neighboring P₆ rings is broken up to form P₁₀ rings (Figure 2j,k). Consequently, a sandwiched structure, consisting of alternating buckled phosphorus sheets with P₁₀ rings and wave-

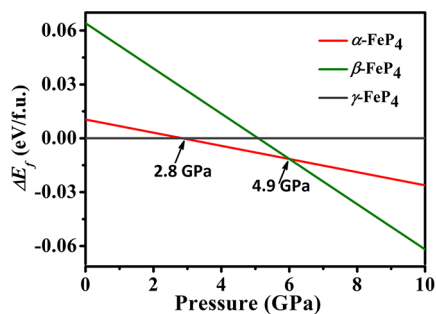


Figure 1. Relative formation enthalpies (ΔE_f) of α -FeP₄ and β -FeP₄ with respect to γ -FeP₄ as a function of pressure.

like/planar metal layers, are built for TMP₄ (TM = V, Cr, Mn, and Fe). The different stacking pattern of the layers and sheets is reflected by their individual symmetry. The P atoms in P₁₀ rings are all tetrahedral-coordinated and can be classified into two different groups: one (four P atoms) is covalently bonded with two adjacent P atoms and two TM atoms, and the other (six P atoms) is covalently bonded with three neighboring P atoms and one TM atom.

The packing of the metal atoms is quite different for individual TMP₄ despite of the similar phosphorus layers. In

VP₄/CrP₄, the zigzag chains of V/Cr atoms are extended along [0 0 1] direction with the uniform distance of 3.208/3.119 Å. In MnP₄ with four different modifications, Mn atoms prefer Mn–Mn dimers with distance of 2.899–2.931 Å, and the distances within the dimer are varied within 3.719–4.205 Å. It should be noted that the distance of the Mn–Mn dimers is much longer than the sum of Mn atomic radius (1.27 Å) and that of MnB₄ (2.674 Å) as well.⁴⁴ For FeP₄, trimetric Fe atoms with intradistance of 3.482 Å and interdistance of 4.091 Å are found in α -FeP₄, and also Fe–Fe distance of 4.001 and 3.512 Å are uniformly distributed in β -FeP₄ and γ -FeP₄, respectively, indicating the isolation of Fe atoms in the FeP₄ phases. The greater Fe–Fe distances in FeP₄ structures are even larger than those in the semiconducting tI40-FeB₄ and cP20-FeB₄, the proposed high pressure phases of FeB₄.⁴⁵ The P–P bond lengths in the P₁₀ rings are depicted in Figure 4a. In general, for the P–P bond lengths in the phosphorus sheets, the maximum increases from VP₄ to FeP₄, the minimum is just converse, and the average values show almost no changes. Interestingly, there is no significant variation for the P–P bond lengths in CrP₄, which is in contrast to that in β -FeP₄, well agreement with the shorter TM distance in CrP₄ (Cr–Cr, 3.119 Å) than in FeP₄ (Fe–Fe, 4.001 Å).

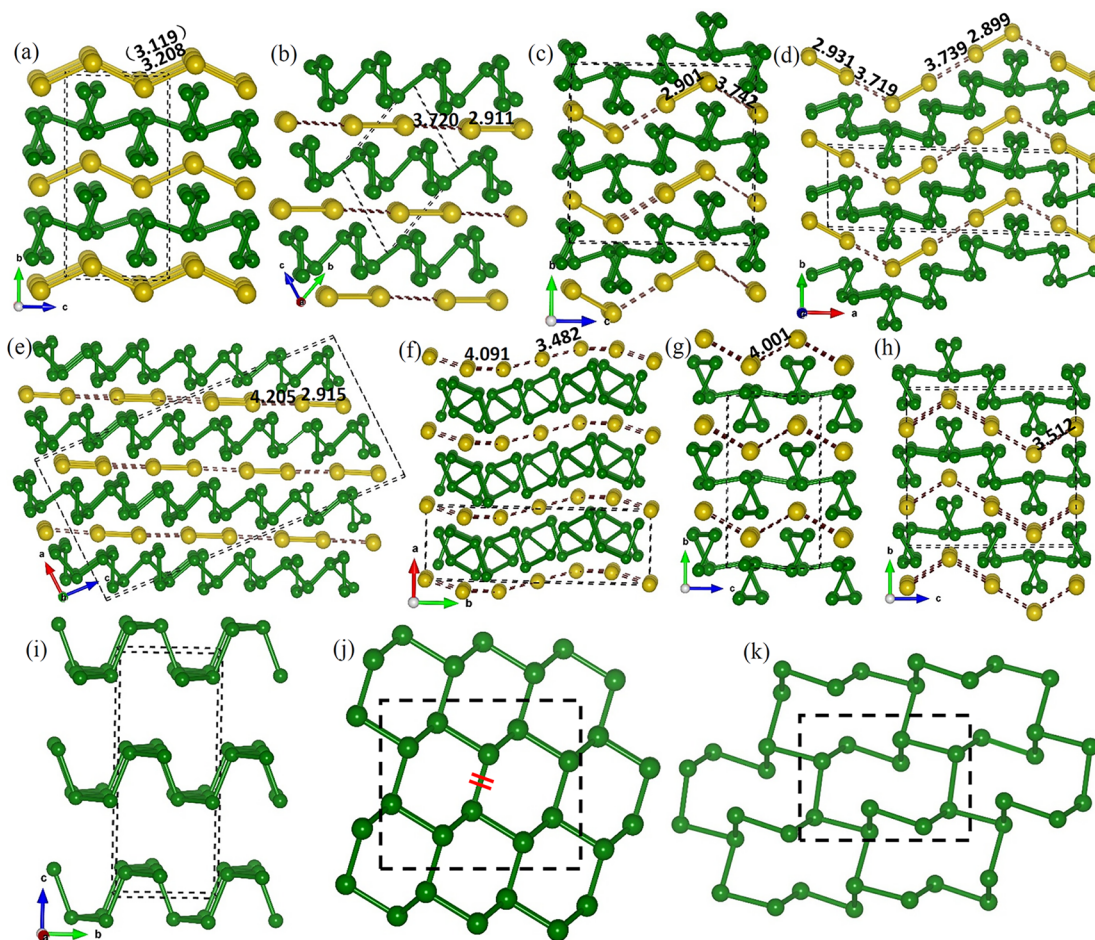


Figure 2. Crystal structures of 3d-TMP₄ (TM = V, Cr, Mn, and Fe): (a) VP₄ or CrP₄ (the value of Cr–Cr bond length is shown in parentheses); (b) 2-MnP₄; (c) γ -MnP₄; (d) 6-MnP₄; (e) 8-MnP₄; (f) α -FeP₄; (g) β -FeP₄; (h) γ -FeP₄. The TM and P atoms are represented as big yellow and small green spheres, respectively. VP₄ is isostructural with CrP₄, so we just show one phase of both isostructural phases here. Panel i shows the black phosphorus crystal structure; panel j shows the phosphorus layer in black phosphorus with P₆ rings, and panel k shows the phosphorus layer in TMP₄ with P₁₀ rings. The structural variation is shown in the two dashed black boxes of panels j and k.

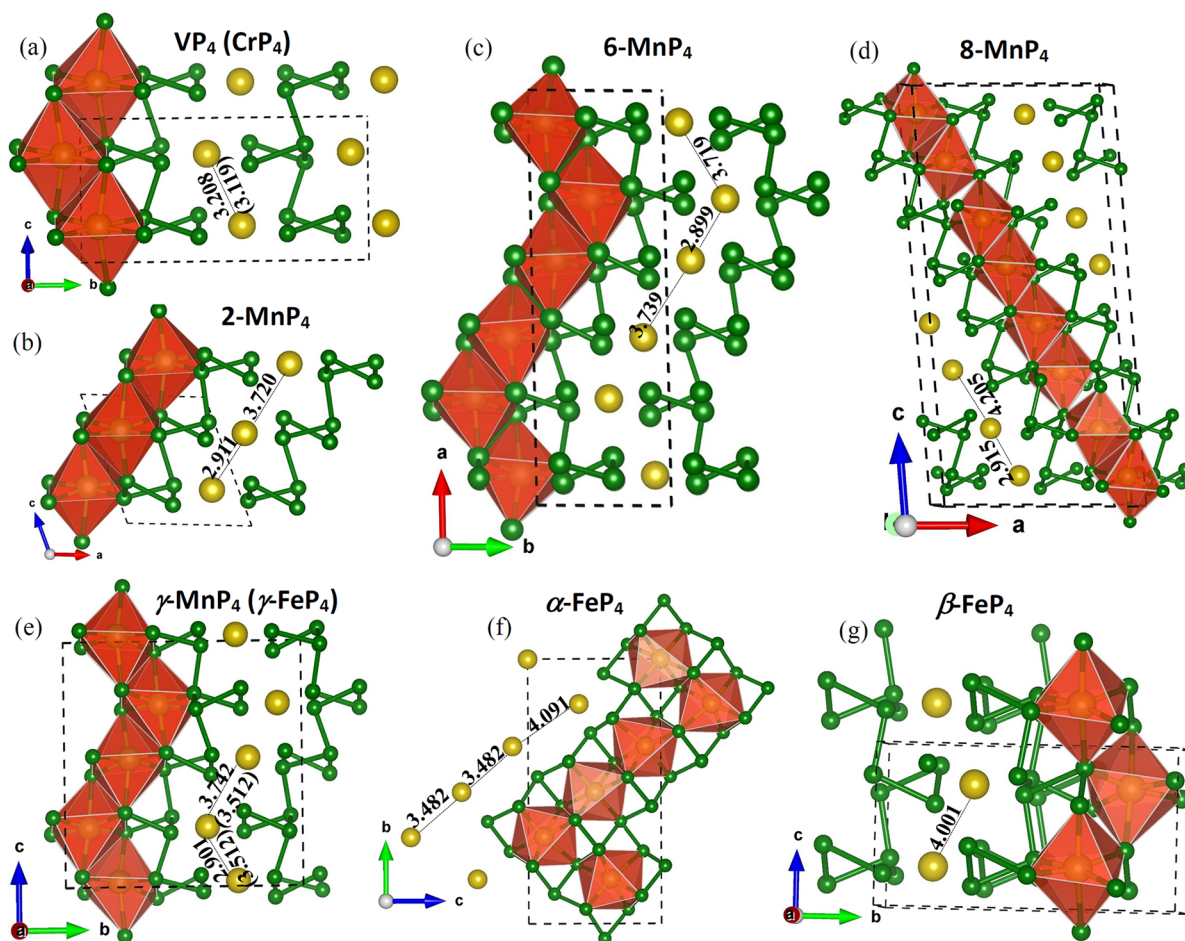


Figure 3. Crystal structures of 3d-TMP₄ (TM = V, Cr, Mn, and Fe) polyhedron view. The TM and P atoms are represented as big yellow and small green spheres, respectively.

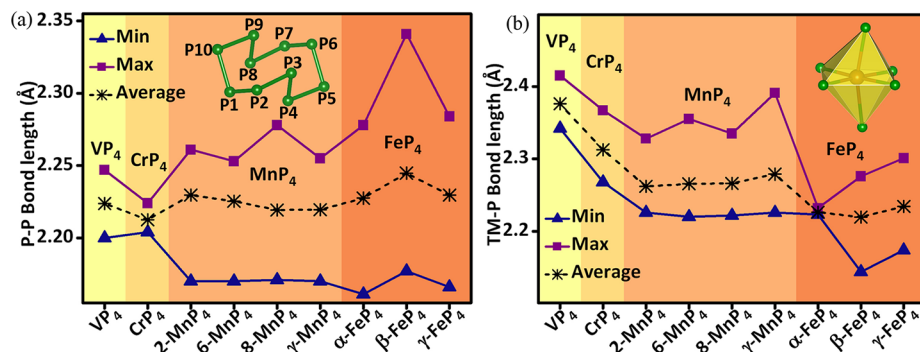


Figure 4. Variation of bond lengths for (a) P–P bonds and (b) TM–P bonds in TMP₄ (TM = V, Cr, Mn, and Fe) phases.

For all the TMP₄ phases, TM atoms are all octahedral-coordinated by six P atoms. Different from the P–P bonds, the average distances of TM–P monotonically decrease (Figure 4b) due to the changes of the metal radius from V to Fe. As shown in Figure 3, edge-sharing TMP₆ octahedrons show the linear arrangements in VP₄, CrP₄, and 2-MnP₄, and wave-like arrangements in 6-MnP₄, γ-MnP₄, and γ-FeP₄. For 8-MnP₄ and α-FeP₄, the TMP₆ octahedrons form TMP₆ groups (four units for 8-MnP₄ and three units for α-FeP₄) by edge-sharing, and the neighboring groups are connected with the corner sharing. Exceptionally, FeP₆ octahedrons in β-FeP₄ are connected together by corner-sharing only.

Electronic Structure. Electronic structures provide a useful clue to explore the origin of the outstanding physical and chemical performance of materials. To analyze the electronic character, the band structure and density of states (DOS) curves of TMP₄ calculated within HSE hybrid function are depicted in Figures 5 and 6. Metallic behavior is observed for VP₄ in good agreement with previous experimental results.¹⁰ The good electronic conductivity of VP₄ suggests the potential applications on the water splitting (HER or OER), just like MoP₂.⁷ For CrP₄, a direct band gap of 0.63 eV is found at the Γ point with the HSE functional; however, the standard PBE calculations give a semimetal character, which is

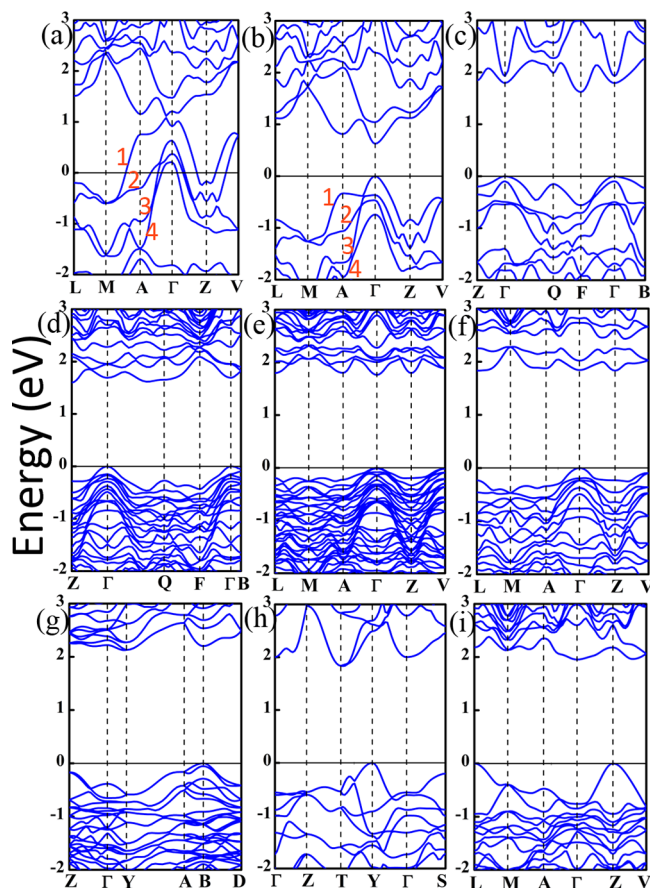


Figure 5. Band structures for (a) VP_4 , (b) CrP_4 , (c) 2-MnP_4 , (d) 6-MnP_4 , (e) 8-MnP_4 , (f) $\gamma\text{-MnP}_4$, (g) $\alpha\text{-FeP}_4$, (h) $\beta\text{-FeP}_4$, and (i) $\gamma\text{-FeP}_4$.

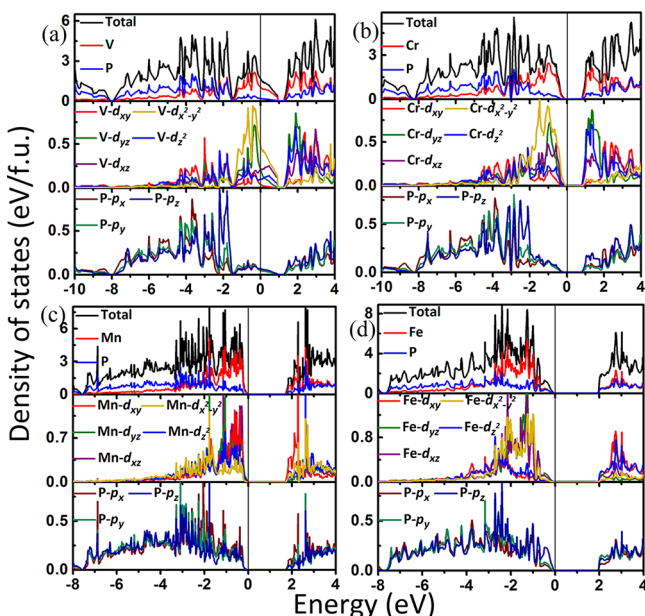


Figure 6. Total and partial density of states for (a) VP_4 , (b) CrP_4 , (c) 6-MnP_4 , and (d) $\gamma\text{-FeP}_4$. The vertical line at zero is the Fermi energy level in DOS photographs.

also suggested in a previous report.²⁹ The calculated band gap of CrP_4 by HSE is comparable to CoP_3 ;^{8,46} excellent bifunctional electrocatalytic activity and durability for HER

and OER were found for the latter.⁴⁷ For MnP_4 , 8-MnP_4 is also a semiconductor with direct band gap 1.76 eV, whereas 2-MnP_4 , 6-MnP_4 , and $\gamma\text{-MnP}_4$ are quasi-direct band gap semiconductors with indirect band gaps of 1.62, 1.60, and 1.83 eV, respectively (see Table 1). The differences between the indirect and direct band gaps at the Γ point are only about 0.17, 0.09, and 0.01 eV, respectively (Figure 5). Furthermore, the calculated band gaps of the different modifications of MnP_4 are very close to each other. All of α -, β -, and $\gamma\text{-FeP}_4$ are indirect band gap semiconductors with equivalent or larger band gaps with those of MnP_4 , 2.13, 1.83, and 1.76 eV, respectively.

As described above, a trend from metal to semiconductor was observed from VP_4 to CrP_4 by HSE methods, although they adopt the same symmetry ($C2/c$) and very similar phosphorus arrangements. The V (Cr) atoms in VP_4 (CrP_4) are uniformly distributed in V (Cr) chains along $[0\ 0\ 1]$ direction with distance of 3.208 (3.119) Å, which is considerably larger than the sum of atomic metallic radius of 1.34 Å for V (1.28 Å for Cr). The metallic interactions between the neighboring V (Cr) atoms are negligible. From Figure 5a,b, the general profile of the energy bands of VP_4 and CrP_4 are very similar, the difference can be observed from the four bands of the 3d electrons (marked 1, 2, 3, and 4) around Fermi level (E_F). The four bands for VP_4 all crossed the Fermi level and are more dispersed in the energy from -1.5 to 1 eV, whereas for CrP_4 , it is compressed in the energy from -2 to 0 eV near the Fermi level. Through DOS analysis (Figure 6a), both the partial densities of states (PDOS) of P and V atoms are prominent at Fermi level, indicating the important interactions between P and V atoms for VP_4 , consistent with no charge density wave phenomenon being observed experimentally, despite the chains of metal atoms extended in the $[0\ 0\ 1]$ direction.²⁹ For MnP_4 and FeP_4 phases, as shown in Figure 5c–i, the energy bands are more depressed and smooth, resulting in larger band gaps opening at E_F .

From density of states (DOS; Figure 6 and Figure S1) for all phases, we can see that DOS of P atoms are analogous to each other due to the similar atomic packing. Furthermore, the almost equal contributions from p_x , p_y , and p_z of P atoms are extended in a wide range from -8 eV to E_F , indicating the strong sp^3 hybridization, which is vital for the stability of phosphorus sheets. Additionally, the hybridizations between P p and TM 3d orbitals can be found in a wide range of the middle energy of the valence band, suggesting a TM–P covalent interaction as well. As focused on the TM atoms, the DOS near E_F of TMP_4 phases are mostly dominated by TM atoms. Although all TM atoms are six-coordinated, forming TMP_6 octahedrons, the 3d orbital degenerations are not identical to each other. More detailed electronic structure of the TM atoms can be obtained by the analysis of PDOS. For VP_4 (Figure 6a), in the energy range of -4.5 and -1.5 eV, the contributions of d_{xy} , d_{yz} , and d_z^2 can be observed, which are hybridized with the P p orbitals, resulting in a V–P covalent interaction. From -1.5 eV to E_F , V d orbitals are most dominant. Especially, the partial atomic orbitals, $d_{x^2-y^2}$, d_{xz} , d_{yz} and d_z^2 contribute to the E_F , whereas the contributions of d_{xy} can be neglected. Moreover, the contribution of $d_{x^2-y^2}$ is distinctly larger than the others. For CrP_4 (Figure 6b), Cr d orbitals are dominant in the energy range of -2 and 0 eV, the contributions of $d_{x^2-y^2}$, d_{xz} , d_{yz} are greater than those of d_{xy} and d_z^2 . Similar phenomena can also be observed for $\gamma\text{-FeP}_4$ (d), 8-MnP_4 (Figure S1b), and $\gamma\text{-MnP}_4$ (Figure S1c). From -2 eV to

E_F in 6-MnP₄ (c), the contributions of d_{yz} , d_{xz} , d_{xy} , and d_z^2 are comparable, and slightly greater than that of $d_{x^2-y^2}$. β -FeP₄ (Figure S1e) is analogous to 6-MnP₄, with the contribution of d_{xy} lower than others. For 2-MnP₄ (Figure S1a), Mn d orbitals also occupy the zone of -2 and 0 eV with contributions of d_{yz} and $d_{xz} > d_{xy}$, $d_{x^2-y^2} > d_z^2$, indicating a different orbital feature of the 3d orbital. α -FeP₄ (Figure S1d) is unique among the TMP₄ phases; the contributions of the partial 3d orbitals of α -FeP₄ are almost equal in the whole valence band zone, indicating that there is no energy splitting in α -FeP₄, in line with the slight difference of the TM bond lengths in FeP₆ octahedrons. Consequently, one can conclude that the different 3d orbital degenerations result from the diverse structural modifications of TMP₄ and hence play a key role in their structural stability.

Distributions of valence electron density provide a further perspective to understand the atomic interactions of these phosphides. As shown in Figure 7 and S2, the remarkable

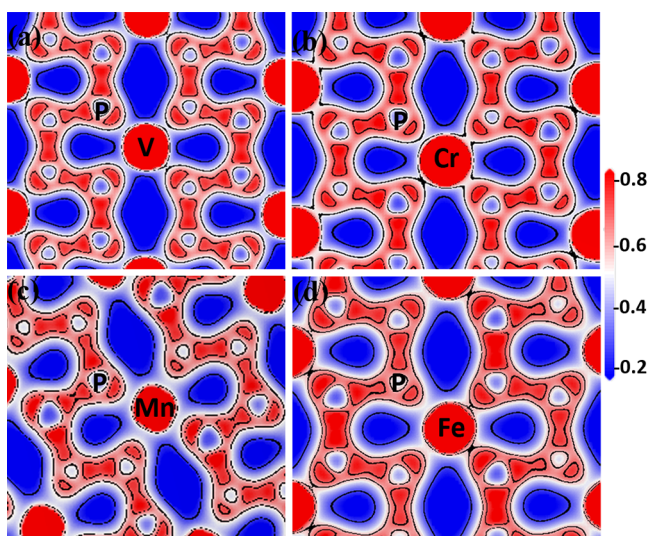


Figure 7. Valence electron density distribution (in $e\text{-}\text{\AA}^{-3}$) for TMP₄ (TM = V, Cr, Mn, and Fe): (a) VP₄, (b) CrP₄, (c) 6-MnP₄, and (d) γ -FeP₄.

electron accumulations for all TMP₄ are revealed between P–P atoms, verifying the covalent P–P interactions in the phosphorus layers, which were also confirmed by the COHP and integrated crystal orbital Hamiltonian population (ICOHP) analysis. A wide bonding state can be observed for P–P from -15 to -3 eV (Figure 8). On the other hand, the electron accumulations between P and TM atoms are also visible (Figure 7 and S2); the bonding states (Figure 8) dominate in almost the whole valence band, further supporting the covalent interactions. The ICOHP of V–P (-3.145), Cr–P (-3.234), and Mn–P (-3.328) are close but higher than Fe–P (-2.901), due to the larger contribution of antibonding states near the Fermi level for γ -FeP₄ than the others. The COHP (ICOHP) for TM–TM in Figure 8, as expected, shows the weaker interactions between the TM atoms and can be neglected, despite the appearance of dimers and trimers in MnP₄ and α -FeP₄. The covalent interactions of P–P in P₁₀ rings and TM–P in TMP₆ octahedrons are further confirmed by the calculated Mulliken overlap populations (MOP). The MOP values of P–P bonds for all TMP₄ phases are within 0.5 – 0.6 , MOP values of TM–P bonds vary significantly, 0.39 – 0.52 for VP₄, 0.41 – 0.58 for CrP₄, 0.22 – 0.50 for MnP₄, and

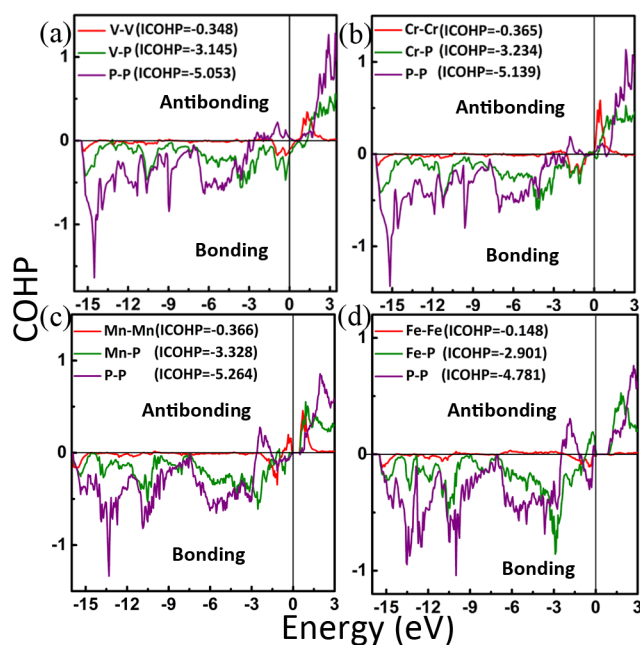


Figure 8. COHP curves and ICOHP values (in eV per pair) for various interatomic interactions in (a) VP₄, (b) CrP₄, (c) 6-MnP₄, and (d) γ -FeP₄.

0.37 – 0.58 for FeP₄ phases. Charge transfer was also observed in TMP₄ by the calculations of Bader charges. A trend of decreasing electron transfer is found, $1.07e$ (VP₄), $0.75e$ (CrP₄), 0.46 – $0.49e$ (MnP₄), and 0.25 – $0.3e$ (FeP₄) are transferred from the TM atom (per TM atom) to phosphorus sheets, which may be due to the increase of the first ionization energy (6.75 eV for V, 6.77 eV for Cr, 7.43 eV for Mn, and 7.90 eV for Fe). Therefore, the degree of ionicity for TM–P bonding decreases from VP₄ to FeP₄.

Mechanical Properties. Mechanical properties are also important for the potential technological and industrial applications. The elastic constants (C_{ij}), bulk modulus (B), shear modulus (G), and Young's modulus (E) are calculated according to Voigt–Reuss–Hill (VHR) methods, listed in Table S1 and Figure 9. C_{33} of VP₄ (191 GPa) and CrP₄ (207 GPa) are remarkably lower than the corresponding C_{11} and C_{22} , indicating more compressibility along the c axis. The C_{11} , C_{22} , and C_{33} of MnP₄ and FeP₄ phases fluctuate in a narrower range, suggesting similar compressive behaviors along a , b and c axes. C_{44} , C_{55} , and C_{66} are closely related to the shear modulus and can be used as a measurement for the shear resistance. As shown in Figure 9, VP₄ possesses the lowest C_{44} (37 GPa), while β -FeP₄ exhibits the largest C_{66} (187 GPa). It is very interesting that for α -FeP₄ the difference of individual elastic moduli is minor, agreeing with the slight difference of Fe–P bond length in FeP₆ octahedron. Furthermore, the calculated B , G , and E , show a slight increase from V to Fe. VP₄ has the lowest B (114 GPa), G (73 GPa), and E (180 GPa), while β -FeP₄ has the largest B (146 GPa), G (129 GPa), and E (299 GPa), which is in good line with ionic characters of the TM–P bonds as described above. Pugh's ratio (B/G) can estimate usually the ductility of materials with a critical value of 1.75 . As listed in Table S1, the B/G values of the all phases are lower than 1.75 , indicating their brittle features. The Poisson's ratio (ν) is also used for evaluation of the directionality of covalent bonding. As listed in Table S1, VP₄ possesses the highest ν (0.24) due to the metallic nature, while the others

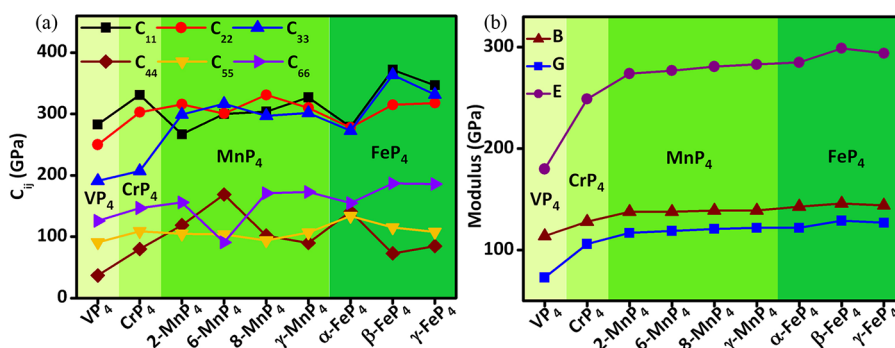


Figure 9. Calculated elastic constants C_{ij} , bulk modulus (B), shear modulus (G), and Young's modulus (E) in TMP_4 ($\text{TM} = \text{V}, \text{Cr}, \text{Mn}, \text{and Fe}$).

adopt similar values because of their semiconducting characters.

CONCLUSIONS

In summary, systematic investigations were performed on the crystal structure, electronic structure, and mechanical properties for 3d TMP_4 ($\text{TM} = \text{V}, \text{Cr}, \text{Mn}, \text{and Fe}$) phases using first-principles calculations based on DFT. TMP_4 are composed of similar buckled phosphorus layers with P_{10} rings and varying metal atomic arrangements: infinite metal chains in VP_4 and CrP_4 , pseudo-Mn–Mn dimers in MnP_4 , and isolated Fe atoms in FeP_4 structures. With a state-of-the-art hybrid functional, VP_4 was confirmed to be metallic, while CrP_4 is a semiconductor with a narrow direct band gap opened at the Γ point. MnP_4 and FeP_4 phases are also semiconducting with varied band gaps, 1.6–2.1 eV. As unveiled by the DOS analysis, the covalent interactions are prominent for both P–P and TM–P bonds, and the different 3d orbital degenerations of the TM atoms play a crucial role in their varied symmetries and structural stability. The results obtained in this work are anticipated to provide good insight and guidance to future experimental investigations on transition-metal phosphides.

ASSOCIATED CONTENT

Supporting Information

The Supporting Information is available free of charge on the ACS Publications website at DOI: 10.1021/acs.inorgchem.8b01380.

Total and partial density of states curves for 2-, 8-, and γ - MnP_4 and α - and β - FeP_4 , valence electron density distribution for 2-, 8-, and γ - MnP_4 and α - and β - FeP_4 , and mechanical properties for TMP_4 ($\text{TM} = \text{V}, \text{Cr}, \text{Mn}, \text{and Fe}$) (PDF)

AUTHOR INFORMATION

Corresponding Authors

*E-mail: wll@ysu.edu.cn.

*E-mail: huiyang.gou@gmail.com.

ORCID

Lailei Wu: 0000-0003-3280-0312

Huiyang Gou: 0000-0002-2612-4314

Faming Gao: 0000-0001-8711-7153

Notes

The authors declare no competing financial interest.

ACKNOWLEDGMENTS

This work was supported by National Natural Science Foundation of China (NSFC) under Grant Nos. 51201148 and U1530402, Thousand Youth Talents Plan, and China Postdoctoral Science Foundation (Grant 2016M601280). We thank Zewen Xiao for useful discussion.

REFERENCES

- Du, H.; Gu, S.; Liu, R.; Li, C. M. Highly active and inexpensive iron phosphide nanorods electrocatalyst towards hydrogen evolution reaction. *Int. J. Hydrogen Energy* **2015**, *40*, 14272–14278.
- Callejas, J. F.; Read, C. G.; Popczun, E. J.; McEnaney, J. M.; Schaak, R. E. Nanostructured Co_2P Electrocatalyst for the Hydrogen Evolution Reaction and Direct Comparison with Morphologically Equivalent CoP . *Chem. Mater.* **2015**, *27*, 3769.
- Popczun, E. J.; McKone, J. R.; Read, C. G.; Biacchi, A. J.; Wiltout, A. M.; Lewis, N. S.; Schaak, R. E. Nanostructured nickel phosphide as an electrocatalyst for the hydrogen evolution reaction. *J. Am. Chem. Soc.* **2013**, *135*, 9267–9270.
- Xiao, P.; Sk, M. A.; Thia, L.; Ge, X.; Lim, R. J.; Wang, J.-Y.; Lim, K. H.; Wang, X. Molybdenum phosphide as an efficient electrocatalyst for the hydrogen evolution reaction. *Energy Environ. Sci.* **2014**, *7*, 2624–2629.
- Son, C. Y.; Kwak, I. H.; Lim, Y. R.; Park, J. FeP and FeP_2 nanowires for efficient electrocatalytic hydrogen evolution reaction. *Chem. Commun.* **2016**, *52*, 2819–2822.
- Liu, M.; Li, J. Cobalt phosphide hollow polyhedron as efficient bifunctional electrocatalysts for the evolution reaction of hydrogen and oxygen. *ACS Appl. Mater. Interfaces* **2016**, *8*, 2158–2165.
- Pu, Z.; Saana Amiin, I.; Wang, M.; Yang, Y.; Mu, S. Semimetallic MoP_2 : an active and stable hydrogen evolution electrocatalyst over the whole pH range. *Nanoscale* **2016**, *8*, 8500.
- Wu, T.; Pi, M.; Wang, X.; Zhang, D.; Chen, S. Three-dimensional metal-organic framework derived porous CoP_3 concave polyhedrons as superior bifunctional electrocatalysts for the evolution of hydrogen and oxygen. *Phys. Chem. Chem. Phys.* **2017**, *19*, 2104.
- Jeitschko, W.; Donohue, P. C. The high pressure synthesis, crystal structure, and properties of CrP_4 and MoP_4 . *Acta Crystallogr., Sect. B: Struct. Crystallogr. Cryst. Chem.* **1972**, *28*, 1893–1898.
- Jeitschko, W.; Flörke, U.; Scholz, U. D. Ambient pressure synthesis, properties, and structure refinements of VP_4 and CoP_2 . *J. Solid State Chem.* **1984**, *52*, 320–326.
- Jeitschko, W.; Rühl, R.; Krieger, U.; Heiden, C. Preparation, properties, and structure refinement of the stacking variant 2- MnP_4 . *Mater. Res. Bull.* **1980**, *15*, 1755–1762.
- Rühl, R.; Jeitschko, W. Stacking variants of MnP_4 : preparation and structure of 6- MnP_4 . *Acta Crystallogr., Sect. B: Struct. Crystallogr. Cryst. Chem.* **1981**, *37*, 39–44.
- Jeitschko, W.; Donohue, P. C. High-pressure MnP_4 , a polyphosphide with Mn–Mn pairs. *Acta Crystallogr., Sect. B: Struct. Crystallogr. Cryst. Chem.* **1975**, *31*, 574–580.

- (14) Henge, D. B.; Hermus, M.; Litterscheid, C. F.; Wagner, N.; Beck, J.; Albert, B.; Brgoch, J. Discovery of γ -MnP₄ and the Polymorphism of Manganese Tetrphosphide. *Inorg. Chem.* **2015**, *54*, 8761–8768.
- (15) Jeitschko, W.; Braun, D. J. Synthesis and crystal structure of the iron polyphosphide FeP₄. *Acta Crystallogr., Sect. B: Struct. Crystallogr. Cryst. Chem.* **1978**, *34*, 3196–3201.
- (16) Sugitani, M.; Kinomura, N.; Koizumi, M.; Kume, S. Preparation and properties of a new iron phosphide FeP₄. *J. Solid State Chem.* **1978**, *26*, 195–201.
- (17) Evain, M.; Brec, R.; Fiechter, S.; Tributsch, H. Crystal structure of a new FeP₄ modification. *J. Solid State Chem.* **1987**, *71*, 40–46.
- (18) Souza, D. C.; Pralong, V.; Jacobson, A. J.; Nazar, L. F. A reversible solid-state crystalline transformation in a metal phosphide induced by redox chemistry. *Science* **2002**, *296*, 2012.
- (19) Doublet, M. L.; Lemoigno, F.; Gillot, F.; Monconduit, L. The Li_xVPn₄ Ternary Phases (Pn: P, As): Rigid Networks for Lithium Intercalation/Deintercalation. *Chem. Mater.* **2002**, *14*, 4126–4133.
- (20) Kim, Y. U.; Cho, B. W.; Sohn, H. J. The Reaction Mechanism of Lithium Insertion in Vanadium Tetrphosphide. *J. Electrochem. Soc.* **2005**, *152*, A475.
- (21) Gillot, F.; Boyanov, S.; Dupont, L.; Doublet, M. L.; Morcrette, M.; Monconduit, L.; Tarascon, J. M. Electrochemical Reactivity and Design of NiP₂ Negative Electrodes for Secondary Li-Ion Batteries. *Chem. Mater.* **2005**, *17*, 6327–6337.
- (22) Boyanov, S.; Bernardi, J.; Bekaert, E.; Ménétrier, M.; Doublet, M. L.; Monconduit, L. P-Redox Mechanism at the Origin of the High Lithium Storage in NiP₂-Based Batteries. *Chem. Mater.* **2009**, *21*, 298–308.
- (23) Silva, D. C. C.; Crosnier, O.; Ouvrard, G.; Greedan, J.; Safa-Sefat, A.; Nazar, L. F. Reversible Lithium Uptake by FeP₂. *Electrochem. Solid-State Lett.* **2003**, *6*, A162–A165.
- (24) Boyanov, S.; Bernardi, J.; Gillot, F.; Dupont, L.; Womes, M.; Tarascon, J. M.; Monconduit, L.; Doublet, M. L. FeP: Another Attractive Anode for the Li-Ion Battery Enlisting a Reversible Two-Step Insertion/Conversion Process. *Chem. Mater.* **2006**, *18*, 3531–3538.
- (25) Pralong, V.; Souza, D. C. S.; Leung, K. T.; Nazar, L. F. Reversible lithium uptake by CoP₃ at low potential: role of the anion. *Electrochem. Commun.* **2002**, *4*, 516–520.
- (26) Alcántara, R.; Tirado, J. L.; Jumas, J. C.; Monconduit, L.; Olivier-Fourcade, J. Electrochemical reaction of lithium with CoP₃. *J. Power Sources* **2002**, *109*, 308–312.
- (27) Demattei, R. C.; Watcharapasorn, A.; Feigelson, R. S. Conditions for the Electrochemical Synthesis of the CoPn₃ (Pn = P, As, Sb) Skutterudites. *J. Electrochem. Soc.* **2001**, *148*, D109–D111.
- (28) Cabana, J.; Monconduit, L.; Larcher, D.; Palacín, M. R. Beyond Intercalation-Based Li-Ion Batteries: The State of the Art and Challenges of Electrode Materials Reacting Through Conversion Reactions. *Adv. Mater.* **2010**, *22*, E170–E192.
- (29) Alvarez, S.; Fontcuberta, J.; Whangbo, M. H. Importance of metal-metal interactions through the phosphorus-phosphorus bonds for the multidimensional electrical properties of MP₄ (M = vanadium, chromium, molybdenum). *Inorg. Chem.* **1988**, *27*, 2702–2706.
- (30) Arbouche, O.; Belgoumène, B.; Soudini, B.; Azzaz, Y.; Bendaoud, H.; Amara, K. First-principles study on structural properties and phase stability of III-phosphide (BP, GaP, AlP and InP). *Comput. Mater. Sci.* **2010**, *47*, 685–692.
- (31) Wang, Y.; Lv, J.; Zhu, L.; Ma, Y. CALYPSO: A method for crystal structure prediction. *Comput. Phys. Commun.* **2012**, *183*, 2063–2070.
- (32) Wang, Y.; Lv, J.; Zhu, L.; Ma, Y. Crystal Structure Prediction via Particle Swarm Optimization. *Phys. Rev. B: Condens. Matter Mater. Phys.* **2010**, *82*, 094116.
- (33) Wang, P.; Wang, Y.; Wang, L.; Zhang, X.; Yu, X.; Zhu, J.; Wang, S.; Qin, J.; Leinenweber, K.; Chen, H.; et al. Elastic, magnetic and electronic properties of iridium phosphide Ir₂P. *Sci. Rep.* **2016**, *6*, 21787.
- (34) Xu, N.; Weng, H. M.; Lv, B. Q.; Matt, C. E.; Park, J.; Bisti, F.; Strocov, V. N.; Gawryluk, D.; Pomjakushina, E.; Conder, K.; et al. Observation of Weyl nodes and Fermi arcs in tantalum phosphide. *Nat. Commun.* **2016**, *7*, 11006.
- (35) Segall, M. D.; Lindan, P. J. D.; Probert, M. J. a.; Pickard, C. J.; Hasnip, P. J.; Clark, S. J.; Payne, M. C. First-principles simulation: ideas, illustrations and the CASTEP code. *J. Phys.: Condens. Matter* **2002**, *14*, 2717.
- (36) Perdew, J. P.; Burke, K.; Ernzerhof, M. Generalized gradient approximation made simple. *Phys. Rev. Lett.* **1996**, *77*, 3865.
- (37) Kresse, G.; Furthmüller, J. Efficient iterative schemes for ab initio total-energy calculations using a plane-wave basis set. *Phys. Rev. B: Condens. Matter Mater. Phys.* **1996**, *54*, 11169.
- (38) Dronskowski, R.; Blochl, P. E. Crystal orbital Hamiltonian populations (COHP): energy-resolved visualization of chemical bonding in solids based on density-functional calculations. *J. Phys. Chem.* **1993**, *97*, 8617–8624.
- (39) Henkelman, G.; Arnaldsson, A.; Jónsson, H. A fast and robust algorithm for Bader decomposition of charge density. *Comput. Mater. Sci.* **2006**, *36*, 354–360.
- (40) Hill, R. The elastic behaviour of a crystalline aggregate. *Proc. Phys. Soc., London, Sect. A* **1952**, *65*, 349.
- (41) Momma, K.; Izumi, F. VESTA: a three-dimensional visualization system for electronic and structural analysis. *J. Appl. Crystallogr.* **2008**, *41*, 653–658.
- (42) Brown, A.; Rundqvist, S. Refinement of the crystal structure of black phosphorus. *Acta Crystallogr.* **1965**, *19*, 684–685.
- (43) Cheng, Y.; Zhu, Y.; Han, Y.; Liu, Z.; Yang, B.; Nie, A.; Huang, W.; Shahbazian-Yassar, R.; Mashayek, F. Sodium-Induced Reordering of Atomic Stacks in Black Phosphorous. *Chem. Mater.* **2017**, *29*, 1350–1356.
- (44) Yang, M.; Wang, Y.; Yao, J.; Li, Z.; Zhang, J.; Wu, L.; Li, H.; Zhang, J.; Gou, H. Structural distortion and band gap opening of hard MnB₄ in comparison with CrB₄ and FeB₄. *J. Solid State Chem.* **2014**, *213*, 52–56.
- (45) Zhang, Y.; Wu, L.; Wan, B.; Zhao, Y.; Gao, R.; Li, Z.; Zhang, J.; Gou, H.; Mao, H. K. Structural variety beyond appearance: high-pressure phases of CrB₄ in comparison with FeB₄. *Phys. Chem. Chem. Phys.* **2016**, *18*, 2361–2368.
- (46) Ackermann, J.; Wold, A. The preparation and characterization of the cobalt skutterudites CoP₃, CoAs₃ and CoSb₃. *J. Phys. Chem. Solids* **1977**, *38*, 1013–1016.
- (47) Wu, T.; Pi, M.; Zhang, D.; Chen, S. 3D structured porous CoP₃ nanoneedle arrays as an efficient bifunctional electrocatalyst for the evolution reaction of hydrogen and oxygen. *J. Mater. Chem. A* **2016**, *4*, 14539–14544.